Tel Aviv University
Raymond and Beverly Sackler Faculty of Exact Sciences
School of Chemistry

Dynamics and diffusion of colloidal particles in an optical vortex

by
Yulia Sokolov

Thesis submitted in partial fulfillment of the requirements for the M.Sc. degree
at Tel Aviv University School of Chemistry

This work has been carried out under the supervision of
Dr. Yael Roichman and Prof. Haim Diamant

February 2011

Contents

Abstract

Holographic optical tweezers can be used to manipulate multiple dielectric particles in designed traps. In this work the trapping pattern is such, that the spherical colloidal particles are driven by constant optical force along a ring-like trap, called a vortex, creating a well-defined, non-equilibrium microscopic system. When several particles are trapped in the vortex, hydrodynamic interactions affect their dynamics, resulting in complex particle motion, including a surprising pairing effect. In this work we examine closely the dynamics of the particles, using experiment, a simple theoretical model, and data from Stokesian Dynamics simulations. We establish the existence of the pairing effect, suggest and confirm its underlying mechanism. We show that the pairing arises from symmetry breaking in the radial positions of the particles, which in turn breaks the symmetry of their pairwise hydrodynamic interactions. We calculate the particles' collective mobilities in different particle density limits, and compare them with experimental average velocities. In addition, we study the random fluctuations of this system, and compare the results to those known in equilibrium systems. We find a crossover in the particles' mean-square displacements along the ring from single-file diffusion at intermediate time to normal diffusion at long time, arising from the collective motion of the assembly.

Chapter 1

Introduction

In this chapter we describe the holographic optical tweezing technique for particle trapping and manipulation, and touch upon the trapping mechanism and particle tracking technique, used in this work. We give a theoretical background for the relevant subjects: (i) hydrodynamics, focusing on the hydrodynamic interactions, or the drag forces the particles apply on each other via the viscous medium; (ii) Stokesian Dynamics simulations, and (iii) diffusion, including single-file diffusion, occurring in 1D or quasi-1D geometries with particles moving in single-file, which is the case for the particles in a vortex.

1.1 Single-particle manipulation

1.1.1 Optical trapping

Optical tweezers (OT) use optical forces exerted by strongly focused laser beams to trap and move objects. Since the forces exerted by light range from femto- to nanonewtons, they can influence the motion of very small, micro- to nanoscale objects [1]. Optical trapping can be described intuitively in two limits: the Rayleigh regime in which $a \ll \lambda$, or the ray optics regime in which $a \gg \lambda$, where a is the trapped particle's radius and λ is the wavelength of the trapping laser beam. Most trapping experiments of dielectric particles are conducted in an intermediate regime where trapped particles are of the order of the wavelength of the trapping beam, which is described more accurately by numerical calculations [2]. The trap can be regarded as a parabolic potential with depth U, which must be larger than the kinetic energy $k_B T$.

In the Rayleigh regime the particle is treated as an induced point dipole in an inhomogeneous electrical field. The force exerted on a particle then consists of two components: the gradient trapping force and the scattering force [3] (see Fig. 1.2).

Each particle feels the Lorentz force

$$\mathbf{F}_{\text{grad}} = (\mathbf{p} \cdot \nabla)\mathbf{E} + \frac{1}{c}\frac{d\mathbf{p}}{dt} \times \mathbf{B}, \tag{1.1}$$

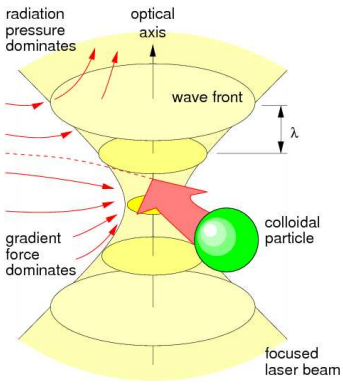

Figure 1.1: Competition between the radiation pressure and the trapping gradient force. For stable trapping the electric gradient force, which attracts the particle to the highest intensity region, must dominate.

where $\mathbf{E}$ and $\mathbf{B}$ are the electric and magnetic fields, $\mathbf{p} = \epsilon\mathbf{E}$ is the particle's dipole and ϵ is the polarizability. In continuous wave laser traps the average gradient force becomes proportional to polarizability

$$\langle \mathbf{F}_{\text{grad}} \rangle = \frac{\epsilon}{2} \nabla \langle \mathbf{E}^2 \rangle , \tag{1.2}$$

and since the square magnitude of the electric filed gives the beam's local intensity, the Rayleigh particle is attracted by the $\mathbf{F}_{\text{grad}}$ to the highest intensity region and gets trapped by it. The scattering force coming from the interaction between electromagnetic wave a small spherical particle is

$$\langle \mathbf{F}_{\text{scat}}(\mathbf{r}) \rangle \propto \epsilon^2 \mathbf{I}(\mathbf{r}) \hat{z}, \tag{1.3}$$

pushing the particle downstream.

In the ray-optics regime transparent particles act as lenses, focusing the light and changing the photon momentum [4]. The momentum transferred from the light to a particle is the difference in linear momentum between incoming and outgoing rays. This momentum is the one that moves the particle towards the focal point.

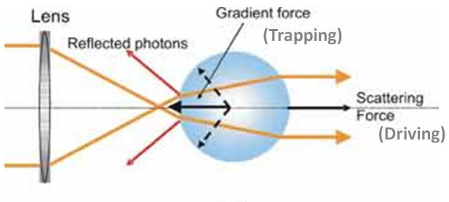

Figure 1.2: The trapping gradient force and the driving scattering force exerted on a particle in a trap.

A typical optical tweezers setup is illustrated in Fig. 1.3 [5]. It comprises a laser source, a beam expander, two stirring mirrors, relay optics and an inverted microscope equipped with a

high NA objective lens. The laser beam is expanded to slightly overfill the back aperture of the microscope's objective lens. It is stirred in two directions by the stirring mirrors and focused by the microscope to create a diffraction limited spot, which is the optical trap.

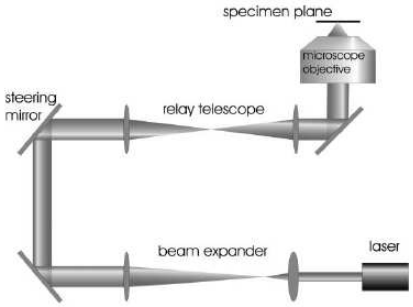

Figure 1.3: Gradient-force optical tweezing set up. A laser beam is expanded, steered onto the microscope port, relayed by a telescope to a high NA microscope objective, slightly overfilling it, and tightly focused onto the sample.

1.1.2 Holographic optical tweezers

In a Holographic Optical Tweezers (HOTs) setup [6, 7] one of the stirring mirrors of a convectional OT setup is replaced with a Spacial Light Modulator (SLM). SLMs are computer controlled devices capable of imprinting a phase-only hologram, a kinoform [8], on the wavefront of a laser beam. When an imprinted beam is focused through an objective lens it forms an image which is related to the Fourier transform of the phase pattern. By calculating specific kinoforms HOTs can be utilized to create multiple optical traps in three dimensions, to change the trap pattern during experiment and to change the nature of the beam [7, 9, 10].

One special beam that can be created with the use of a SLM is the optical vortex. An optical vortex is a beam of light whose phase is given by $\phi = l\theta$ [11], where l is the topological charge of the vortex, the winding number of the azimuthal angle θ. The helical mode is therefore given by:

$$\psi_l(\mathbf{r}) = u(r, z)e^{-ikz}e^{il\theta}, \tag{1.4}$$

where $k\hat{z}$ is the beam's wavevector and $u(r, z)$ is the field's radial profile at position $\hat{z}$. A typical phase hologram of an optical vortex with topological charge $l = 6$ is depicted in Fig. 1.4. This phase pattern has a singular point in its center which causes the beam to interfere destructively. The excess light forms a ring-like trap at a radius directly connected to the vortex's topological charge. As a result, particles are drawn to the ring by intensity gradient forces and are driven with constant force along its circumference by scattering forces [2, 10, 12, 13]. The potential exerted by an optical trap in the radial direction is equivalent to the potential of a Hookean spring.

Most observed characteristics of optical vortices have been interpreted in terms of the properties of Laguerre-Gaussian (LG) eigenmodes of the paraxial Helmholtz equation [14, 15]. These

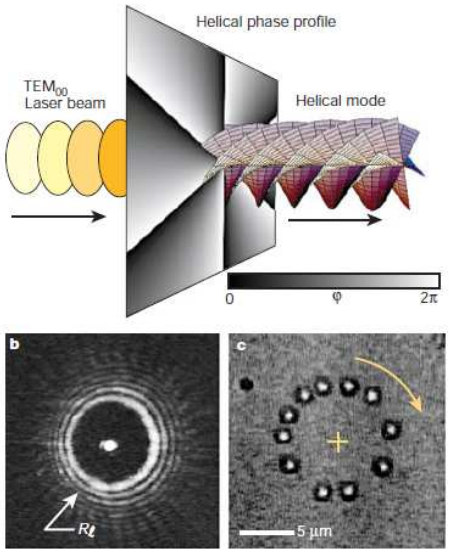

Figure 1.4: The TEM laser beam is projected onto the SLM screen, then each pixel is undergoing a phase shift of $\phi(\rho) = l\theta$, according to a field at each pixel through amorphous Si liquid crystals orientation shift, and transforming from transverse to helical mode. b. The resulting destructive interference along the optical axis, turning a point focused trap to a ring-like trap with radius R_l proportional to topological charge l. c. Trapping colloidal particles with an optical vortex. The particle is caught in an optical angular momentum flux and circling along the circular trajectory.

have a radial dependence

$$u_p^l(r,z) = (-1)^p \left(\frac{\sqrt{2}r}{w}\right)^l L_p^l\left(\frac{2r^2}{w^2}\right) \exp\left(-\frac{r^2}{w^2}\right), \tag{1.5}$$

where L_p^l is a generalized Laguerre polynomial with radial index p , and w is the beam's radius [11]. If each scattered photon is assumed to transfer an angular momentum proportional to $l\hbar$, then the time required to complete one cycle in a vortex should scale as

$$T_l(P) \propto \frac{\sqrt{l}}{P}, \tag{1.6}$$

where P is the power of the input beam of wavelength λ. For $l > l_0$ it is expected that $T_l(P) \propto \frac{l^2}{P}$. The intensity dependence on the arclength s around the ring is modeled as

$$I_l(s) = \frac{P}{2\pi\lambda R_l}. \tag{1.7}$$

The tangential force exerted on a particle in a vortex then is

$$F_l(s) = A_0 \frac{P}{R_l}. \tag{1.8}$$

A_0 is the prefactor including such geometric factors as the particle's scattering cross-section.

1.2 Colloidal dynamics

1.3 Hydrodynamic interaction

In this experiment we deal with a common hydrodynamic problem, colloidal spherical particles moving in water, inducing long-range flows and affecting each other's motion.

1.3.1 Navier-Stokes equations

The basic scenario at hand is the isothermal flow of a homogeneous viscous fluid. In the hydrodynamic regime, where the local properties of the fluid can be regarded as constant on micro-scales, the fluid behavior can be treated phenomenologically with fluid mechanics equations [18], and all the hydrodynamic variables obey matter, momentum conservation laws. The derivation of the fluid motion dynamic equation is based on Newton's laws of motion, interpreted to the following statement: per unit volume, the rate of change of momentum is equal to the rate of momentum increase and loss by convection through the surface, and to the sum of external forces. For incompressible fluids, when the local density of the fluid ρ_{f} is assumed constant, the fluid motion is described by the Navier-Stokes equation [19]:

$$\rho_{\mathrm{f}}\frac{Du}{Dt} = \rho_{\mathrm{f}}\left(\frac{\partial u}{\partial t} + u\nabla u\right) = -\nabla p + \eta\nabla^2 u + \mathbf{F}, \tag{1.9}$$

plus the incompressibility constraint, $\nabla \cdot u = 0$. p is the fluid's hydrostatic pressure, u is the mean fluid velocity, $\mathbf{F}$ is the external force density, and η the dynamic shear viscosity.

When the flow is laminar and sufficiently slow, the inertial effects can be neglected [20]. This behavior is related to the low Reynolds number limit, when

$$Re = \frac{\rho_{\mathrm{f}} v\sigma}{\eta} \ll 1, \tag{1.10}$$

where σ and v are the relevant scales of length and velocity (here, the particle diameter and its velocity). In this limit the problem can be treated with the simpler Stokes or creeping motion equations, which amounts to setting the left-hand size of Eq. (1.9) to zero.

When the Stokes equation with the incompressibility constraint are applied to the motion of an isolated spherical particle, the following Stokes law follows [21]:

$$\begin{aligned} \mathbf{v} &= B_s\mathbf{F}, \\ B_s &= (3\pi\eta\sigma)^{-1}, \end{aligned} \tag{1.11}$$

where $B_s = 1/\xi$ is the particle self-mobility (ξ is the sphere's drag coefficient).

1.3.2 Stokeslet approximation

In this work we describe the hydrodynamic interactions between particles within the simplest Stokeslet approximation. This description strictly holds in the limit of large inter-particle distance relative to the particle size.

The relation between a sphere's velocity $\mathbf{v}$ to the force $\mathbf{F}$ and flow $\mathbf{u}$ it experiences is given by Faxen's law [22]:

$$\mathbf{v} = \mathbf{u}(r) + B_s\mathbf{F} + \frac{\sigma^2}{24}\nabla^2\mathbf{u}(r). \tag{1.12}$$

If no force is exerted on the particle, and if the pressure gradient is small relatively to the particle diameter σ, the sphere can be assumed to be simply advected by the fluid flow, $\mathbf{v} = \mathbf{u}$. On the other hand, a local force $\mathbf{F}(\mathbf{r}_i)$ applied to sphere i induces a flow at large distances, $|\mathbf{r} - \mathbf{r}_i| \gg \sigma$, of the form [23, 24]

$$\mathbf{u}(\mathbf{r}) = \mathbf{O}(\mathbf{r} - \mathbf{r}_i) \cdot \mathbf{F}(\mathbf{r}_i), \tag{1.13}$$

where $\mathbf{O}$ is the Oseen tensor, relating the force to the resulting flow velocity,

$$O_{\alpha\beta}(\mathbf{r}) = \frac{1}{8\pi\eta r}\left(\delta_{\alpha\beta} + \frac{r_\alpha r_\beta}{r^2}\right), \tag{1.14}$$

where $\alpha, \beta = x, y, z$. Combining these two approximate results, we have

$$\mathbf{v}_j = \mathbf{O}(\mathbf{r}_j - \mathbf{r}_i) \cdot \mathbf{F}_i \tag{1.15}$$

This is the so called Stokeslet approximation. It implies that for interparticle distance much larger than particle size, $r \gg \sigma$, the *pair-mobility tensor* is simply given by the Oseen tensor,

$$B_{ij,\alpha\beta}(\mathbf{r}_{ij}) \simeq O_{\alpha\beta}(\mathbf{r}_{ij}), \tag{1.16}$$

where $\mathbf{r}_{ij} = \mathbf{r}_j - \mathbf{r}_i$ is the vector connecting the two particles.

1.3.3 Random motion

Normal and anomalous diffusion

In our experiment, on top of the driven motion of particles through the liquid, we also deal with a very well-known random process, diffusion, with the simplest case of no-memory or a Markov process. The diffusion itself takes place via Brownian motion. Brownian motion of our colloid particles results from collisions with the much smaller medium particles (i.e., water molecules) that surround them. It can be described by either Langevin's phenomenological approach using stochastic theory [25], or by probability distributions using the differential Fokker-Planck equation [26].

In the Langevin treatment of the problem, the overall force acting on a free (undriven and non-interacting) Brownian particle consists of two considerations: a systematic frictional force associated with the slow relaxation of the initial particle velocity due to the viscous drag forces, as described in Sec. 1.3, and a randomly fluctuating force $f(t)$, coming from frequent collisions with the medium, so that

$$m\dot{\mathbf{v}}(t) = -\xi\mathbf{v}(t) + f(t), \tag{1.17}$$

where $\mathbf{v}(t)$ is the particle's velocity, m its mass, and ξ is the friction coefficient. The random force is assumed to have a zero mean, infinitesimally short autocorrelation times and mean-square fluctuations that satisfy the fluctuation-dissipation law, $\langle f(t)f(t+\tau)\rangle = 2k_BT\xi\delta(\tau)$. At sufficiently

long times or in the overdamped limit the inertial forces can be neglected and the mean square displacement (MSD) becomes

$$\langle \Delta r(\tau)^2 \rangle = 6\frac{k_B T}{\xi}\tau. \tag{1.18}$$

The self-diffusion coefficient D is defined as

$$D = \lim_{\tau \to \infty} \frac{\langle \Delta r(\tau)^2 \rangle}{6\tau}, \tag{1.19}$$

and after comparison with Eq. 1.18,

$$D = \frac{k_B T}{\xi}, \tag{1.20}$$

giving Einstein's relation for D in terms of the friction coefficient ξ. And so if Eq. (1.18) is rewritten, we get

$$\langle \Delta r(\tau)^2 \rangle = 6D\tau. \tag{1.21}$$

For a d-dimensional case the expression is

$$\langle \Delta r(\tau)^2 \rangle = 2dD\tau. \tag{1.22}$$

In Eqs. (1.21) and (1.22) the MSD is linearly dependent on time. This behavior is widespread in systems close to equilibrium and is referred to as normal diffusion [27]. In this case the solution of the diffusion equation has the Gaussian form and the next conditions are fulfilled: the variable increments have a defined and finite mean and variance, are mutually independent and the number of steps is large.

There are many systems which do not follow this pattern, but diffuse either slower or faster than in the normal diffusion case. The diffusion processes are characterized through the scaling of the MSD with time. If the general scaling is

$$\langle r^2(t) \rangle \propto t^{\gamma}, \tag{1.23}$$

then γ is the diffusion scaling index. When $\gamma = 1$, the diffusion is normal, otherwise the diffusion is anomalous and can be either subdiffusion for $\gamma < 1$ or superdiffusion for $\gamma > 1$. This scaling index can be obtained from a linear fit of $log(\langle r^2 \rangle)$ versus $log(t)$ plot.

Single-file diffusion (SFD)

SFD was introduced first in 1955 by Hodgkin and Keynes in relation to particle transport across a membrane [28]. This type of diffusion was studied both experimentally and theoretically since then. It was found, that SFD occurs, when the particles move in a channel, sufficiently narrow to prevent them from passing each other [29, 30, 31]. The scaling index typical for SFD equals 1/2, and the expression for MSD is

$$\langle r^2(t) \rangle = F_{\mathrm{sf}}\sqrt{t}, \tag{1.24}$$

where F_{sf} is the SFD mobility. It was found that constricting the particles to a one-dimensional sequence leads to a scaling index of 1/2 [30]. Thus, SFD offers perhaps the simplest example of

subdiffusion. Levitt pointed that this scaling should be expected in most physical systems, where the frequency of the collisions with random background is much larger than the inter-particle collision frequency, for example, when the particles move through narrow water-filled pores [31].

Experiments with the colloids diffusing in quasi- 1D circular channels [32] show the existence of crossover time t_c from normal self-diffusion for $t < t_c$ to SFD for $t > t_c$. In this study the hydrodynamic interactions between the particles could be neglected because the distance between the particles was sufficiently large. For weakly interacting colloidal spherical particles in 1D grooves, diffusion depends on the interaction time t_i [33]. When $t < t_i$, which is approximately equal to the average collision time between the spheres, normal diffusion was observed. It was found, that the scaling index γ decreases as the time increases, until reaching 1/2 for $t \gg t_i$, the onset of subdiffusion. The crossover from normal self-diffusion to SFD depends on the particle density. As the particle density increases, interaction time between the particles decreases, reducing the crossover time.

The SFD mobility $F_{\rm sf}$ for colloidal systems can be determined by the short-time collective diffusion coefficient [34],

$$F_{\rm sf} = \frac{S}{\rho}\sqrt{\frac{D_{\rm col}}{\pi}}, \tag{1.25}$$

where $S = S(q = 0)$ is the zero-wavevector structure factor, equal to the relative compressibility of the 1D particle assembly, ρ its average 1D density, and $D_{\rm col}$ its zero-wavevector effective diffusivity. This equation holds for relatively low concentrations [35], when hydrodynamic interactions are sufficiently weak. The way to calculate the prefactor in the presence of strong hydrodynamic interactions is still unknown.

Colloidal particles trapped in a quasistatic (non-driving) optical circular trap show the same behavior: gradual transition from normal self-diffusion with $\gamma = 1$ at short-time to SFD with $\gamma = 1/2$ at long-time [36]. In that work crossover time and SFD mobility were measured as a function of particle density, showing that both crossover time and prefactor $F_{\rm sf}$ decrease with particle density. The measured $F_{\rm sf}$ values were also compared to the theoretically predicted mobilities by Eq. (1.25). To our knowledge SFD has never been studied for driven particles.

1.3.4 Stokesian Dynamics simulation

Brownian Dynamics is a common technique to simulate systems of particles that obey the Langevin equation, (Eq. 1.17), including interparticle interactions. Stokesian Dynamics is an extension of this technique that takes into consideration hydrodynamic interactions [37]. Thus, these simulations include: stochastic Brownian motion (see Sec. 1.3.3), inter-particle interactions (if the particles interact directly), and many-body hydrodynamic interactions (see Sec. 1.3). In Sec. 1.3 we described a way to deal with hydrodynamic interactions using the so-called Stokeslet approximation. In Stokesian Dynamics simulations a more accurate approximation is used, taking into consideration the size of the particles, via the so-called Rotne-Prager tensor [42] instead of the Oseen tensor.

Chapter 2

Technical details

In this chapter we supply experimental and simulation technical details, and describe the data analysis for (i) experimental and simulation average velocities and (ii) experimental mean square displacement calculations.

2.1 Experimental system

We use holographic optical tweezers to trap and drive colloidal particles along the ring of light. We image the particles' motion with an optical microscope and track their positions. We extract the coordinates from the movies for analysis and study of the particles' dynamics and diffusion.

Our sample consists of a water dispersion of colloidal polystyrene particles with diameter $\sigma = 1.48 \pm 0.08$ μm (Bangs Laboratories Inc. PS04N), encapsulated between a glass microscope slide and a coverslip.

We use holographic optical tweezers (HOT), described in Sec. 1.1.2, to create an optical vortex, by imprinting a helical phase profile on a laser beam (Coherent Verdi, $\lambda = 532$ nm) with a Hamamatsu X6750 PPM spatial light modulator. A Nikon TE-2000U inverted optical microscope with an oil immersion Plan-Apo objective lens (100× NA 1.4) is used both to focus the laser light and to image the trapped particles. The laser light focuses in the sample plane into a ring of light of diameter $2R = 12.41 \pm 0.06$ μm.

Particles are trapped in the vortex by radial gradient forces and are propelled in the tangential direction due to phase gradients in the helical beams of light [38]. Adaptive optics methods are employed to ensure a near-constant tangential driving force, F_θ [39, 40]. By tuning the particle size and radius of the vortex we restrict the particles to one-dimensional, single-file motion.

A series of experiments with the number of trapped particles ranging from $N = 1$ to $N = 16$ was performed. The motion of the particles was recorded on a Pioneer 520H-S digital video recorder (DVR) with a NEC TI-324AII monochrome video camera at a rate of 30 frames per second and the particle positions were extracted with 20 nm resolution by applying digital video analysis, as

described in the next section.

We optimize the combination of such parameters as the size of the particles, vortex radius, the trap intensity and the distance of the lens from the coverslip with the sample. These parameters define how well the particles are trapped, and the maximum particle density on the ring.

2.2 Particle tracking

After recording the images of the particles. We use the well known particle tracking algorithm of Crocker and Grier [17]. Initially each image is filtered to clean high frequency and low frequency noise. The local maxima of brightness in the image are located. From this list the intensity peaks resulting from particles are chosen, and their exact location is deduces by a fit to a 2D Gaussian. After all images are analyzed thus, particle motion and identity are calculated using a least squares method.

We use the data files including particle number, frame number and particle's position after making sure that the location and tracking give reasonable results. After we have those we proceed with the calculations described in the next section.

2.3 Data analysis

We are interested in the average particle velocities for various particle numbers and in mean square displacements (MSD) for various number of steps τ, $\langle \Delta r^2 \rangle(\tau)$. We translate the cartesian coordinates that we get after tracking the particles to polar coordinates. We then calculate the displacements of the particles along the vortex circumference and in the radial direction. We approximate the arc to be a straight line, when the angular step is sufficiently small, and the radial step to be a normal to the tangential step (see Fig. 2.1).

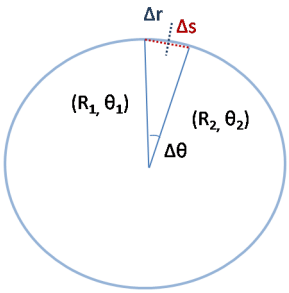

Figure 2.1: Calculation of MSD for particles on a ring.

The displacements in the tangential and the radial directions are then

$$\Delta s = \frac{2R_1R_2\sin\Delta\theta}{\sqrt{R_1^2R_2^2 + 2R_1R_2\cos\Delta\theta}}, \tag{2.1}$$

$$\Delta r = \frac{R_2^2 - R_1^2}{\sqrt{R_1^2R_2^2 + 2R_1R_2\cos\Delta\theta}}. \tag{2.2}$$

We average over Δs to get the average velocities.

Mean square displacement is a statistical value, demanding repetition of the same experiment, in the same conditions, for each time interval. This is hard to achieve experimentally. Assuming the system to be ergodic [1] we analyze the data derived from one experiment, breaking it to many independent time intervals for each step number τ, as demonstrated for a 2D-random walk in Fig. 2.2. We calculate the displacements Δs and Δr per τ, averaging over the number of intervals t_{tot}/τ, where t_{tot} is the total number of frames. Then we follow the usual routine, calculating $[\langle\Delta s^2\rangle - \langle\Delta s\rangle^2](\tau)$ or the variance $var(\Delta s)$ and in the same manner $var(\Delta r)$.

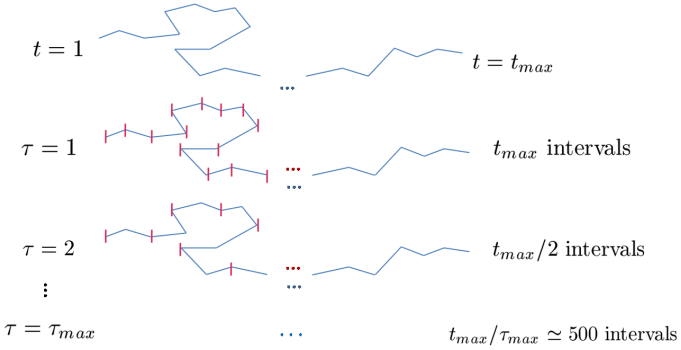

Figure 2.2: Two-dimensional random walk. One experiment is broken to several for varying $\tau = [1, \tau_{max}]$.

2.4 Simulation details

All the simulations were programmed and run by Derek Frydel. Stokesian Dynamics are used to simulate the driven colloidal particles in an optical vortex [37]. The radial degree of freedom is assumed to have an impact on the system's behavior. Therefore in this simulation the particles are restricted to two-dimensional motion, while confined in the radial direction to a ring of radius $R = 5\sigma$ (σ being the particle's diameter) by a harmonic radial potential of spring constant k_r. A constant tangential force $F^\theta = Rk_\theta$ is driving the particles around the ring, and a repulsive WCA pair interaction [41] prevents them from overlapping. Hydrodynamic interactions between particles are modeled using the many-body Rotne-Prager mobility tensor [42]. Temperature is introduced

[1] In ergodic system all the microstates have the same probability over a long period of time. In this case, the average of a variable over time can be assumed to be the same as the average over the statistical ansemble.

via a Gaussian-distributed random force, obeying the fluctuation dissipation relation using the same mobility tensor. The temperature in the simulation is presented in units of $k_\theta \sigma^2/k_\mathrm{B}$, where k_B is Boltzmann's constant, and the angular velocity in units of $B_\mathrm{s} k_\theta$, where $B_\mathrm{s} = (3\pi\eta\sigma)^{-1}$ is the particle's self-mobility in a liquid of viscosity η. The data analysis of the simulation results for extraction of the average velocities is equivalent to the experimental one.

Chapter 3

Results and discussion

Colloidal particles driven in an optical vortex exhibit complicated dynamics, expressed through fluctuating distances between them and various transient particle arrangements, such as pairs or trains, forming and breaking as the particles circulate along the vortex. For example, in Fig. 3.1 (a) and (b) we see the same two particles with two different angular distances between them. It means that their velocities are not constant, despite the approximately identical optical force exerted on them.[1] In addition, we observe particle pairing, as shown in Fig. 3.1 (b). The particles come close to one another, move in a pair, split, then pair again, exhibiting quite peculiar behavior for non-interacting particles. We see this pairing effect in the angular distance distribution (see Fig. 3.2), where the average inter-particle distance is fluctuating around 35°. As the particle number increases, the picture becomes more complicated, but common features are observed in all the vortices: the inter-particle distances fluctuate and there is a tendency to create pairs and even short-lived chains.

We see the pairing effect manifestation in Fig 3.3, where there is a clear difference between the average particle velocity in odd or even particle rings. The stronger correlations in the even case, where all the particles can be paired, lead to increased collective mobilities, due to drag reduction. In the odd particle number case there is always at least one unpaired particle, leading to lower velocities than the adjacent even N.

Another feature seen in Fig. 3.3 is the average velocity non-monotonous increase, unlike what is usually observed in particles moving in single-file in a channel. The reason for this common observation is the fact that a train of particles experiences less drag than its constituent particles would feel when isolated. Why then is it not the case for the particles moving in single-file in the vortex?

[1] It is important to note, that the vortex is not an ideal circle, but slightly elliptical. In addition, the intensity is not homogeneous, due to the optical setup inaccuracies. For the case of homogeneous distribution the same force is exerted on the particles, whereas inhomogeneity leads to slight deviations in the force applied on each particle. It becomes important when studying and understanding both dynamical and random behavior of the particles. Nevertheless, in our theoretical model and during the analysis we assume the vortex to be a perfect ring and the driving force to be identical for all the particles and constant. Our primary motivation here is to identify the effects that are insensitive to such imperfections.

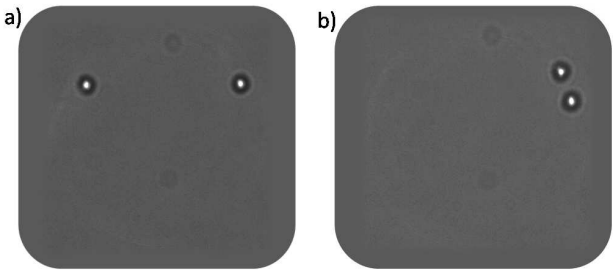

Figure 3.1: Two-particle vortex with (a) separated and (b) paired particles.

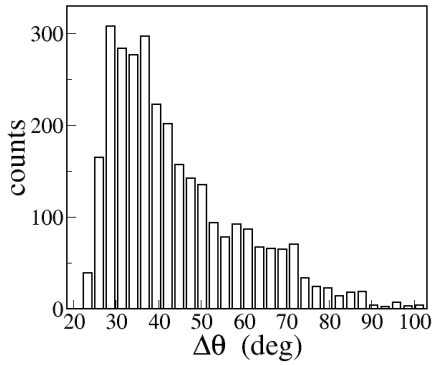

Figure 3.2: Distribution of experimentally measured angular distances between particles in a two-particle vortex. The particles form a long-lived pair with a fluctuating but well defined separation angle.

3.1 The pairing mechanism

Since the driving force is approximately identical and constant for all the particles, and the particles should have no intrinsic interactions other than short-range hard-core ones, we suspect that the hydrodynamic interactions could be responsible for the observed dynamics. We see in our theoretical calculations that hydrodynamic interactions in the radial direction could be responsible for the pairing (See Sec. 4.2). We therefore propose a pairing mechanism based on radial symmetry breaking, as schematically depicted in Fig. 3.4. Under a tangential optical driving force on two particles in a vortex the leading particle is shifted to a slightly larger radius, $R_1 > R$, and a trailing particle to a slightly smaller one, $R_2 < R$. Once the symmetry is broken, the trailing particle's angular velocity becomes higher than that of the leading particle. As a result the trailing particle catches up with a leading one. As the particle number increases, each one of the particles will affect the others, giving rise to complicated dynamics, as observed in the experiments.

Plotting the distribution of leading and trailing particle radii ratio R_1/R_2 in Fig. 3.5, we

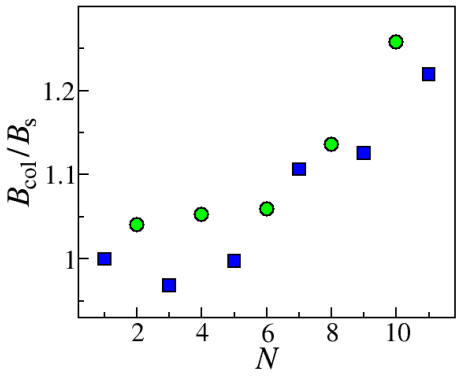

Figure 3.3: Average particle velocities plotted versus particle number N, showing the difference between odd (blue squares) and even (green circles) particle number dynamics. The average particle velocity is scaled by the velocity in a single-particle vortex. This is also equal to the ratio between the collective mobility of particles in the vortex and their self-mobility as isolated particles.

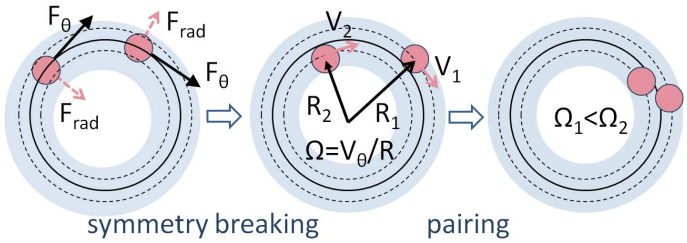

Figure 3.4: The pairing mechanism. As optical forces drive the particles along the ring, the resulting fluid flow pushes the leading particle outward and pulls the trailing one inward. Once displaced radially, the particles' angular velocities change, making the trailing particle catch up with the leading one.

see that it is biased toward values larger than 1, proving that the leading particle adopts a higher radius trajectory.

In Fig. 3.6 we see the same result from simulation, under low temperature and weak radial confinement conditions. The distribution of the leading particle's radius has higher values than that of the trailing one, in a circular trap under constant driving force with sufficiently weak radial confinement. The angular distance between particles in a pair under these conditions is found to be about 13°. Hence, the symmetry breaking is borne out by the statistics of the measured trajectories, as we propose.

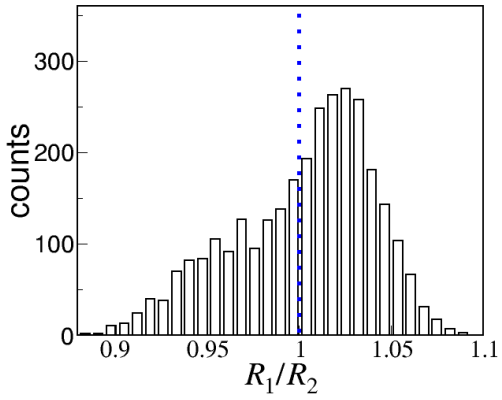

Figure 3.5: Distribution of the experimentally measured ratio between the radii of the leading and trailing particles in a two-particle vortex.

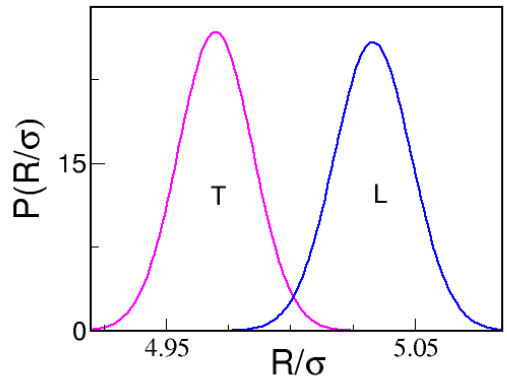

Figure 3.6: The radii distributions of the leading (L) and the trailing (T) particles in a simulated vortex. The leading particle's mean radius is higher than that of the trailing particle, pointing at the radial symmetry breaking.

3.1.1 Collective mobility

We have already observed the effect of pairing on the average velocity in vortices containing even versus odd number of particles (Fig. 3.3). In Fig. 3.7 we further compare the experimentally measured average velocities for even N with the theoretical collective mobilities predicted by Eq. (4.11) for paired particles driven in a ring, using a vertical shift α as a fitting parameter

[1]. Despite the oversimplified model, described in detail in Sec. 4.3.1, a reasonable agreement is obtained for $\alpha = 1.10 \pm 0.02$. Largest deviations are obtained for $N = 2$ and 4, which are systems characterized by low particle density, and therefore more affected by noise.

At given experimental conditions the particles are not fixed in one configuration, as in our theoretical model, but switching between several transient configurations [43, 44], and since the average velocity depends on statistical sampling of these configurations, it becomes stochastic. For $N = 2$, for example, the theoretically considered paired configuration is the fastest one. In practice, the noise increases the average inter-particle distance, and therefore reduces the overall mobility relative to the theoretical one of a fixed pair. For $N = 4$, conversely, the theoretically considered configuration of two opposing pairs is relatively slow, since the pairs inhibit each other via the fluid medium. In this case thermal noise causes the particles to sample faster configurations, reducing the hindrance effect and increasing the collective mobility. At this point, as one of the reasons for positive mobility deviation, a pairing between two pairs was considered, which indeed takes place in certain conditions. This configuration was seen in simulations by Derek Frydel [44], along with other stable configurations that the four particles can adopt.

We see the same behavior in the simulations, as presented in Fig. 3.8. We analyzed the simulation data in two different temperatures to show the thermal effect on the average particle velocities in the dilute rings. In Fig. 3.8 the particle collective velocity for $N = 4$ at $T = 0.02$ is higher than at $T = 0.1$, as a result of the configuration that the particles adopt. These configurations are temperature and confinement dependent [44], therefore, in a given radial confinement, temperature dictates the particle arrangement on a ring, and therefore, their dynamic properties, such as collective mobilities. For $N > 4$ the simulation results agree with our theoretical prediction with fitting parameter $\alpha = 1.57 \pm 0.05$.

The value of $\alpha = B_{\mathrm{p}}/B_{\mathrm{s}}$ can be related to the inter-particle distance through the theoretical expression for the mobility of a pair of spheres [45]. In the simulation we measure an angular distance of $\Delta\theta = 12.9 \pm 0.1°$, which corresponds to $\alpha = 1.52 \pm 0.02$. These two independent measurements of α agree within the statistical error.

In both experiment and simulation, as the particle number increases, the number of possible configurations and the particle density on a ring also increase. It leads to smaller deviations from the theoretically considered positions, and a better agreement with the theoretical prediction. For particle numbers higher than 4 we observe the usual mobility increase with increasing N. This tendency is broken when reaching the maximum density on a ring. At this density, the particles begin to wander outside the vortex, as shown in Fig. 3.9. In this experiment the maximum density is $\phi_{max} = N\sigma/(2\pi R) = 0.38 \pm 0.02$, for $N = 10$.

In Sec. 4.3.2 we propose that the driven particles in such a dense ring in this limit should be comparable to that of a driven torus, leading to a linear average velocity dependence on particle number.

We now understand that the average velocity dependence on increasing particle number is affected by hydrodynamic interactions, temperature, radial confinement, particle configurations and the particle density. This leads to the non-monotonous behavior seen in Figures 3.3, 3.7 and

[1]The exact definition of the collective mobility is described in Sec. 4.3.1. Here it is sufficient to note that the collective mobility in our system is equal to the measured average velocity divided by the tangential driving force.

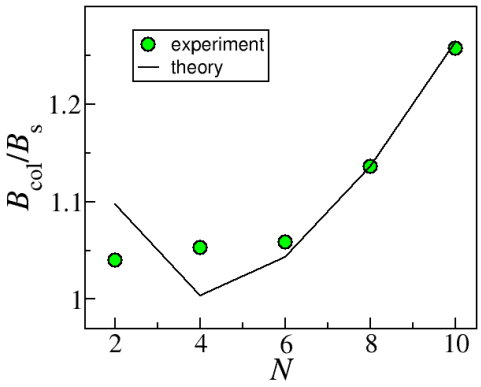

Figure 3.7: Experimental results for the particle velocity (scaled by the velocity in a single-particle vortex) for even N along with the theoretical prediction [Eq. (4.11)] with $\alpha = 1.10 \pm 0.02$ (solid line). Experimental error bars are smaller than symbols.

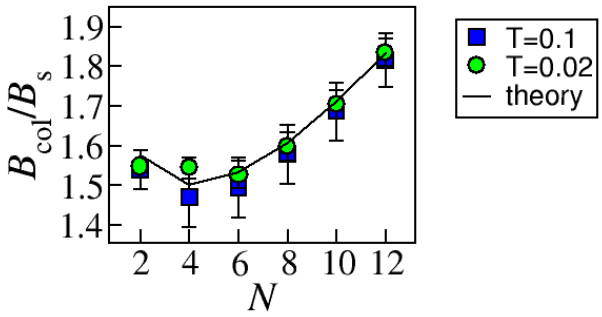

Figure 3.8: Simulation results for particle velocity (scaled by the velocity in a single-particle vortex) at T=0.02 (green circles) and T=0.1 (blue squares) for even N along with the theoretical prediction [Eq. (4.11)] with $\alpha = 1.57 \pm 0.05$ (solid line).

3.8.

3.1.2 Diffusion

On top of the system dynamics, the particles also perform random fluctuations within the available radial and tangential degrees of freedom, both of which are discussed below. We calculate and plot the mean square displacements of the particles' fluctuations (to be distinguished from their driven

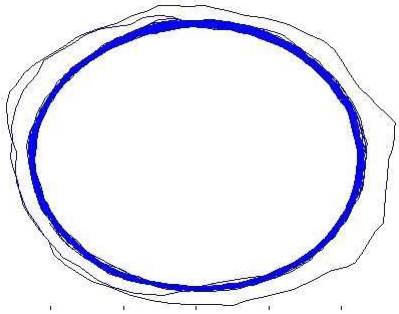

Figure 3.9: The trajectory of one of the particles in an N=12 ring. The particle is pushed out of the ring due to high particle density. It happens when $N > 10$, or $\phi > \phi_{max} \simeq 0.38$.

motion) using the procedure described in Sec. 2.3.

Example of the resulting logarithmic plot of $\langle \Delta s^2 \rangle$ versus τ is shown in Fig. 3.10. Note that these variances are supposed to eliminate the effect of the deterministic driven motion of the particle around the ring. We will see, however, that this is not exactly the case. After examination of all the particles in different N-ring plots, a consistent pattern is seen: linear trends with three different regions, perturbed by periodic wiggles. The crowding of these wiggles (to be discussed shortly) on the long-time logarithmic scale allows us to average over them and perform a linear fit in regions 2 and 3. We take into consideration the inaccuracy in separation into regions by eye, and extract scaling index γ values from the slope, while averaging over the selected approximate regions, as demonstrated in Fig. 3.11. This procedure is performed for each particle number, ranging between $N = 1$ and $N = 13$ and for each particle in each vortex. Then the results are averaged over all the particles per each N. This analysis was applied for both experiment and simulation. The logarithmic plot for $\langle \Delta r^2 \rangle$ is shown in Fig. 3.12.

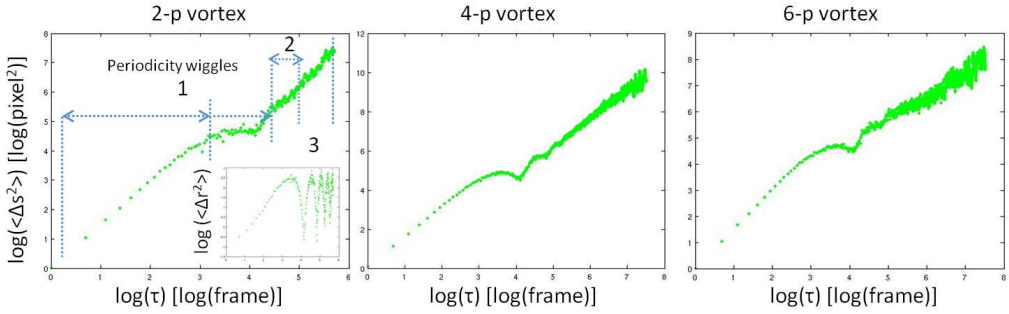

Figure 3.10: Log-log plots of mean square displacement in tangential and radial (inset) directions vs time.

In Fig. 3.10 region 1 is not analyzable, since what we see there is a single wiggle — a result of the periodical deterministic motion of the particle around the ring. The period of the highest peak on the Fourier transform plot fits the period it takes the particle to complete a cycle (see

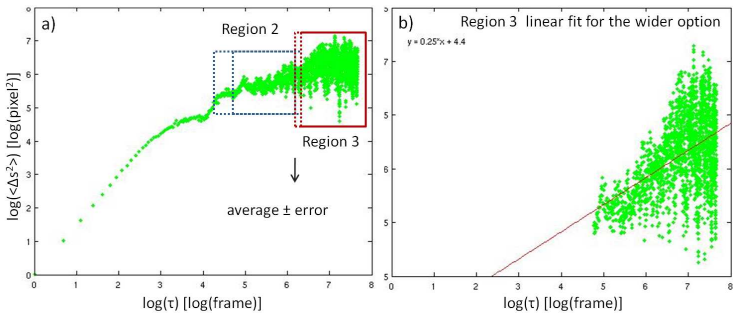

Figure 3.11: Example of log-log $\langle \Delta s^2 \rangle$ versus τ plot for one of the particles in 8-particle vortex. (a) Example how the regions are chosen and (b) Linear fit to the data in the chosen region.

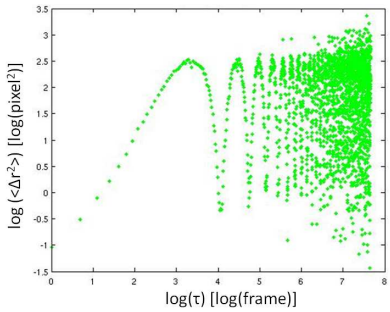

Figure 3.12: Example of log-log $\langle \Delta r^2 \rangle$ versus τ plot for one of the particles in 8-particle vortex.

Fig. 3.13). For example, the highest peak in the FT plot for each particle in a three-particle vortex, gives the period of 67 frames, and this is exactly the number of frames it takes each particle to complete one loop in a vortex. We therefore conclude, that the vortex intensity inhomogeneity is responsible for the wiggles in the MSD plots.

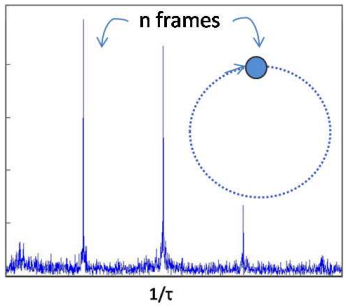

Figure 3.13: Example of Fourier transform plot of the $\langle \Delta s^2 \rangle$. The high peaks originate from the wiggles seen in MSD log-plots.

In Fig. 3.14 we see the results for the scaling exponent γ for even [panels (a) and (b)] and odd [(c) and (d)] particle number. For even N, as the particle number increases, γ asymptotically approximates 0.6 ± 0.2 in region 2 and 1.1 ± 0.1 in region 3. For odd N no consistent pattern is observed. This is again the manifestation of the pairing, leading to the difference in diffusive behavior between odd or even particle number.

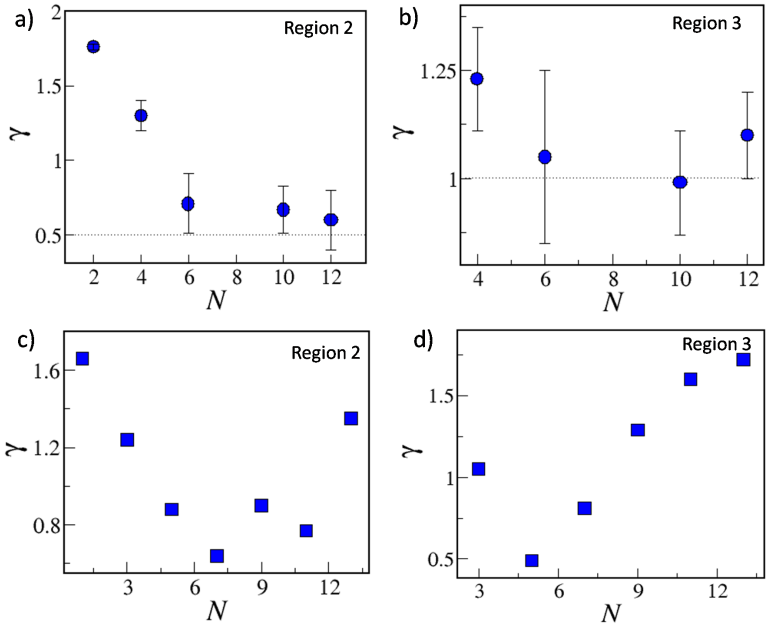

Figure 3.14: Average scaling exponents of the particles as a function of particle number for region 2 (a) and 3 (b), for even N [(a),(b)] and odd N [(c),(d)]. As the particle number increases, γ goes to about 0.5 in region 2 and to about 1 in region 3.

The exponent found for Region 2 is typical of single-file diffusion (SFD), discussed in Sec. 1.3.3. Despite the non-equilibrium conditions, the particles in a vortex also perform quasi-1D SFD. Region 2 is the sub-diffusional area, corresponding to the collisions time-scale, where each particle becomes aware of its closest neighbors reducing its degrees of freedom and leading to the diffusion indices of approximately 0.5. In our experiment the system is small enough to observe the crossover to the center-of-mass diffusion, which is normal. Thus, in region 3 the particles diffuse with $\gamma \simeq 1$, due to reaching the time-scales, where the particles are aware of all the other particles, and exhibit collective behavior. To our knowledge, this is the first time this crossover was observed experimentally. This behavior is relevant for sufficiently high particle densities in a vortex, where the collision times are sufficiently short. We assume, that we do not see SFD features in relatively dilute systems in our set of experiments, since the measurement time is not sufficiently long for the collisions between the particles to become appreciable.

If we compare the radial mean square displacements of the leading and the trailing particles [see Fig. 3.15 (a) and (b)] in a two-particle vortex, we see that the leading particle is periodically

fluctuating with smaller amplitude than the trailing one. This effect reduces the average radii ratio we calculated and plotted earlier in Fig. 3.5.

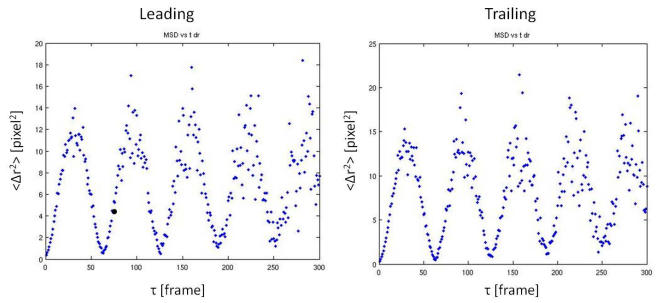

Figure 3.15: Radial MSD of the leading (a) and the trailing (b) particle in a two-particle vortex. The radial fluctuation amplitude of the leading particle is smaller than that of the trailing particle, pointing at the subtle intensity profile influence on the radial distribution discussed in Sec. 3.1.

3.2 Summary

In this chapter we discussed the pseudo pair-attraction between the particles in a vortex, seen in both experiments and simulations. We suggested the mechanism for particle pairing based on radial symmetry breaking, and supported by the radial distribution and collective dynamics, combining experiment, simulation and theory. We found that dilute rings are affected by strong noise. From four particles on, the mobility continuously increases, as we predicted theoretically, up to a maximum occupied fraction ϕ_{max}. At this and higher densities two problems occur: (i) the particles begin to get out of the trap and wander nearby ; (ii) the Stokeslet approximation no longer holds and so does our model. The high-density region could not be examined due to problem (i). We predict theoretically, in the next section, that in this limit the collective mobility is expected to be linearly dependent on the particle number.

In addition, we examined the particle diffusion in the tangential and radial directions. We found that the particle pairing influences the random fluctuations of the system as well, manifesting itself through the difference between odd and even particle number. For even particle numbers we find a crossover from SFD to collective normal diffusion. For odd particle numbers no consistent pattern was observed. Wavy patterns seen in the MSD plots were examined through Fourier transform and related to the trap intensity inhomogeneity.

Chapter 4

Theory

In addition to direct interactions (if there are any), particles in a viscous fluid medium interact hydrodynamically. In this chapter we discuss hydrodynamic interactions between the particles in an optical vortex, using a simplified analytical model to describe the system. We suggest a mechanism for the pairing observed in experiment and simulation, and discussed in Sec. 3.1. We calculate the collective mobilities, and examine their dependence on the particle density in the ring.

4.1 The mobility tensor

Hydrodynamic interactions could give rise to the pair attraction observed in the experiment. We therefore build a rough model to describe the experimental system, and check how hydrodynamic interactions influence the particle dynamics.

We assume that colloidal particles motion in water is overdamped, and obeys the stick boundary condition at the particle surface. Therefore, Stokes law can be applied, and the self-mobility coefficient of a single particle is given by

$$B_s = (3\pi\eta\sigma)^{-1}, \tag{4.1}$$

where η is the liquid viscosity and σ the particle diameter.

We use the Stokeslet approximation to describe the hydrodynamic interactions (see Sec. 1.3.2). The distance between the particles, in fact, may not be large enough to ignore the particles size influence. Thus the Stokeslet approximation fits the real picture very roughly. This approximation becomes even less appropriate for the particles coming close to create a pair. Nevertheless, we use the Oseen tensor to build a many-body mobility tensor and calculate the particle velocities in the tangential and radial directions. For two isolated particles the change in the velocity of one particle, $\Delta\mathbf{v}$, due to a force $\mathbf{F}$ acting on the other, is given within the Stokeslet approximation by

$$\Delta\mathbf{v} \simeq \mathbf{O} \cdot \mathbf{F}, \tag{4.2}$$

where $\mathbf{O}$ is the Oseen tensor, defined in Eq. (1.14).

For N particles the velocity–force relation is

$$\begin{pmatrix} \mathbf{v_1} \\ \mathbf{v_2} \\ \vdots \\ \mathbf{v_N} \end{pmatrix} = \begin{pmatrix} \mathbf{B}_{11} & \mathbf{B}_{12} & \cdots \mathbf{B}_{1N} \\ \mathbf{B}_{21} & \mathbf{B}_{22} & \cdots \mathbf{B}_{2N} \\ \vdots & \vdots & \ddots \\ \mathbf{B}_{N1} & \cdots & \cdots \mathbf{B}_{NN} \end{pmatrix} \begin{pmatrix} \mathbf{F}_1 \\ \mathbf{F}_2 \\ \vdots \\ \mathbf{F}_N \end{pmatrix}, \tag{4.3}$$

where the matrix defines a many-particle mobility tensor, and the $\mathbf{B}_{ij}$'s are in principle functions of the positions of all particles. The Stokeslet approximation then implies that we replace each $\mathbf{B}_{ii}$ by $B_{\mathrm{s}}\mathbf{I}$, where $\mathbf{I}$ is the identity matrix, and each $\mathbf{B}_{ij}$, $i \neq j$, by $\mathbf{O}(\mathbf{r}_{ij})$, where $\mathbf{r}_{ij}$ is the vector connecting particles i and j. Thus the velocity of particle i is the superposition of the velocities resulting from its self-mobility and pairwise interaction with all the other particles $j = 1...N$, $j \neq i$,

$$\mathbf{v_i} = B_{\mathrm{s}}\mathbf{F}_i + \sum_{j=1, j\neq i}^{N} \mathbf{O}(\mathbf{r}_{ij}) \cdot \mathbf{F_j}. \tag{4.4}$$

Since the particles in the experiment are moving along a planar circular trajectory, we set the plane of motion at $z = 0$ and translate the tensor coordinates from cartesian $(x, y, z = 0)$ to polar $(r = R, \theta, z = 0)$, where R is the ring's radius, using the azimuthal projection operator $\hat{\theta} = (-\sin\theta, \cos\theta)$. For each term in Eq. (4.4) then

$$\begin{aligned} x_{ij} &= R(\cos\theta_j - \cos\theta_i), \\ y_{ij} &= R(\sin\theta_j - \sin\theta_i), \\ |r_{ij}|^2 &= 2R^2[1 - \cos(\theta_{ij})], \end{aligned} \tag{4.5}$$

where $\theta_{ij} = \theta_j - \theta_i$. Now we can substitute the results into Eq. (4.4) and calculate the tangential and radial velocities of the particles.

We now focus on two particles. According to the experimental situation we restrict the following analysis to driving forces that are purely tangential,

$$\mathbf{F}_j = F_j\hat{\theta} \tag{4.6}$$

This tangential force on particle j can change velocity of particle i in both tangential and radial directions. We begin with the tangential component of the particle i velocity resulting from particle j motion. Using Eqs. (4.4) and (4.5), we get

$$\begin{aligned} v^{\theta} &= [B_{\mathrm{s}} + G^{\theta\theta}(\theta_{ij})]F^{\theta}, \\ G^{\theta\theta} &= \frac{1 + 3\cos\theta_{ij}}{16\pi\eta R\sqrt{2(1 - \cos\theta_{ij})}}, \end{aligned} \tag{4.7}$$

where $\theta_{ij} = \theta_j - \theta_i$.

Similarly, in the radial direction we get

$$\begin{aligned} v^r &= G^{r\theta}(\theta_{ij})F^{\theta}, \\ G^{r\theta} &= \frac{3\sin\theta_{ij}}{16\pi\eta R\sqrt{2(1-\cos\theta_{ij})}}. \end{aligned} \tag{4.8}$$

4.2 The pairing mechanism

Now we check how hydrodynamic interactions in any of the directions can be responsible for the pairing effect observed in the experiment. The simplest case to look at is a pair of spherical particles on a ring, separated by an angular distance $\theta_{ij} = \theta_j - \theta_i$. Equation (4.7) is symmetric under particle exchange, $\theta_{ij} \to \theta_{ji} = -\theta_{ij}$. This means that, in the tangential direction, particles i and j pull each other in the same direction and with the same strength. Therefore, the tangential coupling cannot account for the pairing effect.

We take into consideration, that in experiment the confining radial force of the vortex is not infinitely strong, therefore allowing the particles a radial degree of freedom. In the absence of the radial trap, this would lead to the radial velocity, given in Eq. (4.8). The fact that Eq. (4.8) is antisymmetric under particle exchange implies, that the hydrodynamic coupling has opposite effects on the radial motions of the two particles. If particle i pushes particle j out of the ring, in the radial direction, particle j pulls it inside the ring (or vice versa). This leads to slightly shifted trajectories in the presence of the radial confining potential (See Sec. 3.1).

The pairing makes the dynamics of odd number of particles more complex than that of even, since in the odd particle number case there will always be one single slower particle, which will be caught up by those paired (see Fig. 4.1)[13, 43]. We focus on the simpler case of even particle number from now on.

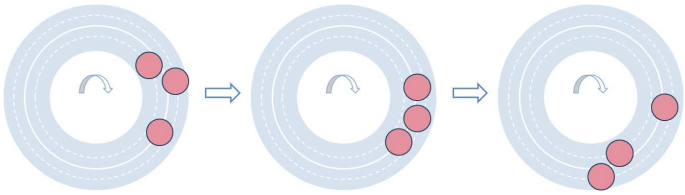

Figure 4.1: Three particles exchanging configurations, as an example of odd particle number behavior.

4.3 Collective mobility for even particle numbers

4.3.1 Collective mobility calculation

An additional way to support the pairing is to look at the collective mobilities in the tangential direction and compare them with the experimental average particle velocities. We first build a

simple model, fixing N unpaired particles to positions evenly distributed along the ring, as shown in Fig. 4.2.

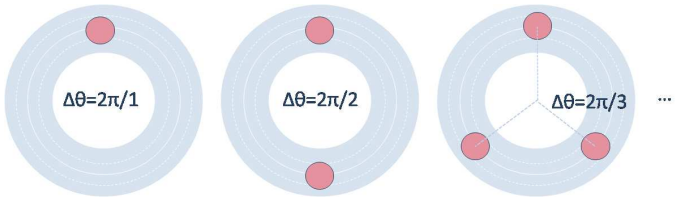

Figure 4.2: The idealized configuration: particles evenly spread along the ring.

In the absence of hydrodynamic interactions each particle moves with tangential velocity $v^\theta = B_\mathrm{s} F^\theta$. The angular distance between each two particles θ_{ij} is now constant and defined by $2\pi/N$. In the tangential direction

$$\begin{pmatrix} v_1^\theta \\ v_2^\theta \\ \vdots \\ v_N^\theta \end{pmatrix} = \begin{pmatrix} B_\mathrm{s} & G^{\theta\theta}(1\cdot 2\pi/N) & G^{\theta\theta}(2\cdot 2\pi/N) & \cdots & G^{\theta\theta}((N-1)\cdot 2\pi/N) \\ G^{\theta\theta}(1\cdot 2\pi/N) & B_\mathrm{s} & G^{\theta\theta}(1\cdot 2\pi/N) & \cdots & G^{\theta\theta}((N-2)\cdot 2\pi/N) \\ \vdots & \vdots & \ddots & \vdots & \vdots \\ G^{\theta\theta}(1\cdot 2\pi/N) & G^{\theta\theta}(2\cdot 2\pi/N) & \cdots & \cdots & B_\mathrm{s} \end{pmatrix} \begin{pmatrix} F_1^\theta \\ F_2^\theta \\ \vdots \\ F_N^\theta \end{pmatrix}, \tag{4.9}$$

where $G^{\theta\theta}(\theta)$ has been defined in Eq. (4.7).

One of the eigenvectors of this mobility tensor has the form $(1, 1....1)$, the collective eigenvector. In simple words, this vector describes the state, when all particles are subjected to the same force and, since they are evenly distributed, move with the same velocity. The existence of this eigenvector is guarantied by our model conditions: identical particles with identical intervals between them, symmetrically positioned on a ring. Hence, the expression for the collective mobility can be found by diagonalization of the tensor in Eq. (4.9) and finding the collective eigenvalue B_col.

It is easy to see that this eigenvalue is simply equal to the sum of row elements of the matrix in Eq. (4.9) (which is equal for all rows). This gives

$$\frac{B_\mathrm{col}}{B_\mathrm{s}} = \frac{v^\theta(N)}{v^\theta(1)} = 1 + B_\mathrm{s}^{-1} \sum_{n=1}^{N-1} G^{\theta\theta}(2\pi n/N). \tag{4.10}$$

To relate this result to the experiment, we now consider two paired particles as an *effective single particle*. The ring then contains N/2 such effective particles, evenly distributed, as shown in Fig. 4.3. The tangential velocity of an isolated pair is taken to be $v^\theta = B_\mathrm{p} F^\theta$, where $B_\mathrm{p} = \alpha B_\mathrm{s}$ is the mobility of a pair with α being a prefactor of order 1. In this case the collective eigenvalue

becomes

$$\frac{B_{\mathrm{col}}}{B_{\mathrm{s}}} = \frac{v^{\theta}(N)}{v^{\theta}(1)} = \alpha + 2B_{\mathrm{s}}^{-1} \sum_{n=1}^{N/2-1} G^{\theta\theta}(4\pi n/N). \tag{4.11}$$

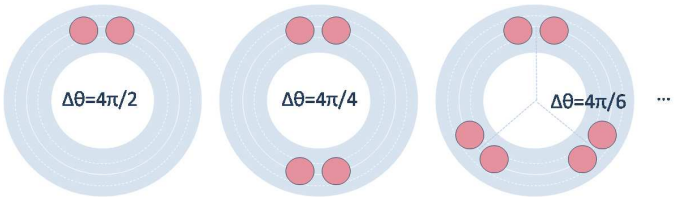

Figure 4.3: The idealized configuration for paired particles, evenly spread along the ring with angular distance $4\pi/N$.

The mobility of an isolated pair of spheres, separated by a given distance and moving along the line that connects them, is known theoretically [45]. Thus, if we know the separation between two particles in a pair, we can predict B_{p}, i.e., the prefactor α (see Sec. 3.1.1).

4.3.2 The particle number influence on their collective mobility

For further calculations we define the occupation fraction $\phi = N\sigma/2\pi R$. In a sufficiently dilute ring, when $\phi \ll 1$, the collective mobility of the particles can be calculated using expressions (4.10) or (4.11), depending on whether we have single or paired particles. The resulting mobility dependence on particle number in the paired case is as shown in Fig. 4.4.

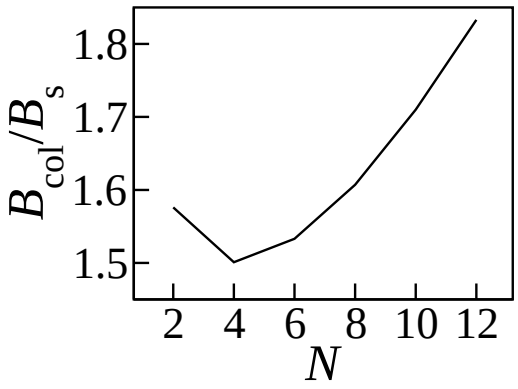

Figure 4.4: Theoretical prediction for mobility dependence on particle number for low occupation fractions. The parameters fit those of the simulation (see Sec. 2.4).

We next check two cases: (i) what happens when the particle density is relatively high; and (ii) what would be the particle collective mobility in the theoretical limit of $N \to \infty$ together with $R \to \infty$ such that ϕ remains small.

The collective particle mobility in a high density ring

For relatively high particle densities, the Stokeslet analysis can no longer be implemented. In this case the particles begin to behave as a dense "train", and the collective mobility should be close to that of a continuous torus.

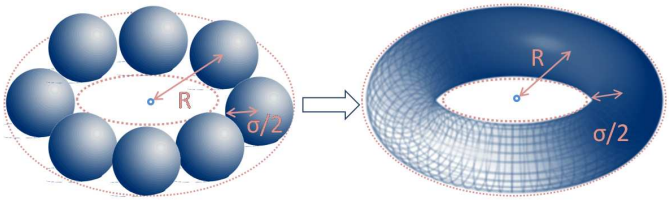

Figure 4.5: High-density ring depicted as an effective torus of a radius R and cross-section radius $\sigma/2$.

If we apply a force F^θ on each particle, then the total force exerted on the torus is NF^θ. Since the collective velocity is equal to each particle velocity and constant, $v^\theta_{\text{torus}} = v^\theta_i \simeq B_{\text{torus}} N F^\theta = B_{\text{col}} F^\theta$, where B_{torus} is the mobility of the torus to rotation around its main axis. Therefore, the particle collective mobility for high density rings is predicted to become linearly dependent on N,

$$B_{\text{col}} \simeq B_{\text{torus}} N. \tag{4.12}$$

The infinite N limit

First of all, how can the $N \to \infty$ theoretical limit be obtained theoretically? If we take a ring of radius R, we can reach this limit by taking infinitely small σ. Thus, we can place many particles on a given circumference. On the other hand, it is just the same, if we fix σ and take infinitely large radius R. We therefore consider again the ratio $N\sigma/R \sim \phi$. As long as this ratio is very small, we can take the particle number to ∞ and still stay in the Stokeslet limit. Since $\Delta\theta$ is defined as $2\pi/N$, the change in the argument of the $G^{\theta\theta}(\theta_{ij})$ between consecutive summation terms in Eq. (4.10) becomes very small. We then can convert the sum $\sum_{n=1}^{N-1} G^{\theta\theta}(2\pi n/N)$ to an integral using Riemann sum:

$$\sum_{n=1}^{N-1} G^{\theta\theta}(2\pi n/N) \simeq \int_0^N G^{\theta\theta}(2\pi n/N)\, \mathrm{d}n. \tag{4.13}$$

Substituting the expression for $G^{\theta\theta}$ from Eq. (4.10) and performing the integration, we get the expression for the mobility:

$$B_{\text{col}} = B_{\text{s}} \left[1 + \frac{3\phi}{2} \left\{ \ln\left(\frac{4\phi R}{\sigma} \right) - \frac{3}{2} \right\} \right] \tag{4.14}$$

As $N \to \infty$, $R/\sigma \to \infty$, while ϕ remains constant. We therefore can simplify expression (4.14) to

$$B_{\mathrm{col}} \simeq \frac{3B_{\mathrm{s}}\phi}{2} \ln\left(\frac{4\phi R}{\sigma}\right). \tag{4.15}$$

According to Eq. (4.15) the collective mobility diverges logarithmically with system size. This behavior is known from other hydrodynamic problems such as the mobility per unit length of a long rod.

Finally, let us look at the mobility of the entire train of particles. To go from a description of N particles with N forces exerted on them to a single train with a single force acting on it, we need to divide the collective mobility of the particles by their number N,

$$B_{\mathrm{train}} = \frac{B_{\mathrm{col}}}{N} = \frac{1}{4\pi^2\eta R} \ln\left(\frac{4R\phi}{\sigma}\right) \tag{4.16}$$

This expression is remarkably similar to the expression for the mobility of a solid cylinder of length $2\pi R$ and radius $\sigma/2$ [46]:

$$B_{\mathrm{cylinder}} = \frac{1}{4\pi^2\eta R} \ln\left(\frac{1.95\pi R}{\sigma}\right). \tag{4.17}$$

We no longer see the effect of the trajectory's curvature due to the ring expansion ($R \to \infty$) in order to keep the ring dilute. But we also see that in this limit, apart from a logarithmic correction, the dilute system behaves as a dense one, pointing at the long-range effect of the hydrodynamic interactions.

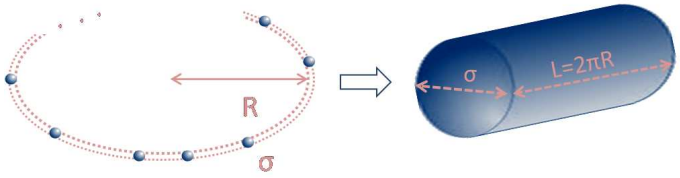

Figure 4.6: According to the similarity of Eqs. (4.16) and (4.17), both the shape of the particles and the curvature of the trajectory become negligible in the $N \to \infty$ limit.

4.4 Summary

In this chapter a simple analytical model was built to describe the experimental system, i.e. colloidal particles moving on a circular trajectory. The Oseen tensor was translated to polar coordinates, and the many-body mobility tensor was calculated for tangential and radial components of particle motion. It was shown, that the radial degree of freedom can be responsible for the pairing effect seen in the experiments. The collective mobility eigenvalue was found for even particle number N, giving the expression for collective mobility as a function of N.

Then the dependence of the collective mobility on the particle density was examined. The region of finite N and low occupation fractions was checked. The mobility for rings with high

particle density was approximated to that of a torus, resulting in a prediction of linear dependence of the collective mobility on N. Both of these predictions can be checked experimentally. In this work we were able to check only the first.

The collective mobility for the theoretical $N \to \infty$ limit was calculated, within the Stokeslet approximation. It was shown that it diverges logarithmically with increasing particle number. The expression itself was found to be almost identical to the expression for the mobility of a solid cylinder.

Chapter 5

Summary and future directions

In this work we studied the deterministic and random behavior of the colloidal particles driven in an optical vortex generated by holographic optical tweezers. Naively, the trapping mechanism implies that the particles should move with constant and identical velocities. But this is not what we observe in the experiments, where particles obviously move with different and changing velocities and also exhibit pair-attraction, unexpected due to the lack of intrinsic long-ranged interactions between them. We therefore set out to examine the system more closely. We focused on both the driven dynamics and diffusion of the particles.

We confirmed the existence of the pairing by (i) the inter-particle angular distances distribution with well-defined separation angle between the particles; (ii) the difference in the average velocity increase with the particle number for rings with odd or even particle number; (iii) the difference in the diffusive behavior of the particles depending on whether N is odd or even; (iv) an agreement between the average particle velocities as a function of particle number and the theoretical collective mobilities of paired particles. The pairing is proved to originate from radial symmetry breaking due to the drag forces via water in the radial direction, by the leading and trailing particles' radii ratio distribution, and by simulations. This mechanism is general, and will work for any system with colloidal particles driven along a curved trajectory with a radial degree of freedom allowed.

We also see that the particle dynamics depends on the particle density in the vortex. It is temperature and radial confinement dependent as well, as was found in simulations by Derek Frydel. Relatively dilute systems are dominated by the hydrodynamic interactions, leading to pairing and various particle configurations, which in turn determine the particles' average velocity. The more dilute the system, the more it is affected by noise. At relatively high particle densities, the system is driven as a rigid structure, which can be compared to a torus. In this experiment we could not strictly observe this limit due to particles being pushed out of the ring when the density is higher than a certain maximum. We predict theoretically, that the average velocity will increase linearly with the particle number. We would like to check this limit experimentally by adjustment of such parameters as the vortex radius and intensity and the particle size.

Since the particles are restricted to move in single-file, their velocities are expected to in-

crease monotonously with the particle number. But considering all the aforementioned parameters influencing the particles' average velocities, we were able to explain why the velocity increase observed in the experimental plot is non-monotonous.

We also derived an expression for the collective mobility in the theoretical $N \to \infty$ limit for dilute rings. This expression is similar to that of a rod, showing that the dilute system behaves much like a dense one. In addition, for $N \to \infty$ the particle mobility diverges logarithmically with N.

We studied the particle diffusion in a vortex, calculating and log-log plotting the mean square displacements in the tangential and radial directions. The diffusion scaling exponent extracted from the mean-square displacements (MSD) indicated that, like particles' diffusion in an equilibrium system [36], the particles in our driven system also undergo single-file diffusion (SFD) over a certain time-range. We observed a crossover from SFD to normal collective diffusion at sufficiently long times, where the center-of-mass diffusion of the entire particle assembly becomes appreciable. This collective regime could be obtained due to the system's small size and the closed trajectory. In addition, the MSD plots revealed the influence of the trap intensity profile on the system's fluctuations. We want to perform more experiments with larger vortices in order to observe the time regime smaller than the collision times, and the crossover times between the regimes, as a function of particle density. We also want to look closer on the odd particle number case. In addition, we are interested in finding the theoretical expression for the prefactors of the single-file MSD in the presence of long-range hydrodynamic interactions and comparing them to experiment.

We would also like to study the non-equilibrium statistical mechanics behind the experimental distributions in this experiment. For example, the apparently exponential distribution of angular separation in a particle pair (Fig. 3.2) may be related to the non-equilibrium features and effective temperature of the system.

Bibliography

[1] A. Ashkin, IEEE j. Sel. Top. Quantum Elec., **61**, 841 (2000)

[2] B. Sun, Y. Roichman and D. G. Grier, Opt. Express, **16**, 15765 (2008)

[3] A. Ashkin, Phys. Rev. Lett., **40**, 729 (1978)

[4] A. Ashkin, Methods Cell Biol.,**55**, 1 (1998)

[5] K. Dholakia, P. Reece and M. Gu, Chem. Soc. Rev.,**37**, 42 (2008)

[6] E. R. Dufresne and D. G.Grier, Rev. Sci. Instrum., **69**, 1974 (1998)

[7] E. R. Dufresne, G. C. Spalding, M. T. Dearing, S. A. Sheets and D. G.Grier, Rev. Sci. Instrum., **72**, 1810 (2001)

[8] L. B. Lesem, P. M. Hirsch and J. A. Jordan,Jr., Opt. Sci. and Tech., **13**, 2, 150 (1969)

[9] J. Liesener, M. Reicherter, T. Haist and H. J. Tiziani, Opt. Commun., **185**, 77 (2000)

[10] J. E. Curtis, B. A. Koss and D. G. Grier, Opt. Commun., **207**, 169 (2002)

[11] L. Allen, M. W. Bejersbergen, R. J. C. Spreeuw, J. P. Woerdman, Phys. Rev. A, **45**, 8185 (1992)

[12] J. E.Curtis and D. G. Grier, Phys. Rev. Let., **901**, 133901 (2003)

[13] Y. Roichman, G. M. Zaslavsky and D. G. Grier, Phys. Rev. E, **75**, 020401(R) (2007)

[14] M. E. J. Friese, J. Enger, H. Rubinstein-Dunlop and N. R. Heckenberg, Phys.Rev. A **54**, 1593 (1996); N. B. Simpson, K. Dholakia, L. Allen and M. J. Padgett, Opt. Lett., **22**, 52 (1997)

[15] A. T. Oneil, I. MacVicar, L. Allen and M. J.'Padgett, Phys. Rev. Lett., **88**, 053601 (2002)

[16] S. Inoue, *Video Microscopy* (New York, Plenum, 1986)

[17] J. C. Crocker and D. G. Grier, J. Colloid Interface Sci., **179**, 298 (1996)

[18] L. D. Landau and E. M. Lifshitz, *Fluid Mechanics*, 2nd Edition, Sec.$\tilde{2}$3, p. 44-83; J. Happel and H. Brenner, *Low Reynolds Number Hydrodynamics* (Martinus Nijhoff, The Hague, 1983), Sec. 2, p. 23-47

[19] J. Happel and H. Brenner, *Low Reynolds Number Hydrodynamics* (Martinus Nijhoff, The Hague, 1983), Sec. 2.1, p. 27

[20] J. Happel and H. Brenner, *Low Reynolds Number Hydrodynamics* (Martinus Nijhoff, The Hague, 1983), Sec. 1.1, p. 3

[21] J. Happel and H. Brenner, *Low Reynolds Number Hydrodynamics* (Martinus Nijhoff, The Hague, 1983), Sec. 2.6, p. 42

[22] J. Happel and H. Brenner, *Low Reynolds Number Hydrodynamics* (Martinus Nijhoff, The Hague, 1983), Sec. 5.11, p. 227

[23] http://physics.nyu.edu/grierlab/leshouches2/node15.html

[24] C. W. Oseen, *Neuere Methoden und Ergebnisse in der Hydrodynamic* (Leipzig: Akademische Verlag, 1927)

[25] P. Langevin, Comptes Rendus de l'Academie des Sciences, **146**, 530 (1908)

[26] H. Risken, *The Fokker-Planck Equation* (Springer-Verlag, Berlin, 1989), 2nd ed.

[27] L. Vlahos, H. Isliker, Y. Kominis and K. Hizanidis, e-print arxiv:0805.0419

[28] A. L. Hodgkin and R. D. Keynes, J. Physiol., **128**, 61 (1955)

[29] J. Karger, Phys. Rev. A, **45**, 4173 (1991); Phys. Rev. E, **47**, 1427 (1992);

[30] S. Alexander and P. Pincus, Phys. Rev. B, **18**, 2011 (1978)

[31] D. G. Levitt, Phys. Rev. A, **8**, 3050 (1973)

[32] Q.-H. Wei, C. Bechinger and P. Liederer, Science, **287**, 625 (2000)

[33] B. Lin, B. Cui, J.-H. Lee and J. Yu, Europhys. Lett., **57**, 724 (2002)

[34] M. Kollman, Phys. Rev. Lett., **90**, 180602 (2003)

[35] B. Lin, M. Meron, B. Cui and S. Rice, Phys. Rev.Lett., **94**, 216001 (2005)

[36] C. Lutz, M. Kollman and C. Bechinger, Phys. Rev. Lett., **931**, 026001 (2004)

[37] J. F. Brady and G. Bossis, Ann. Rev. fluid Mech., **20**, 111 (1988)

[38] Y. Roichman, B. Sun, Y. Roichman, J. Amato-Grill and D. G. Grier, Phys. Rev. Let., **100**, 013602 (2008)

[39] M. Polin, K. Ladavac, S. H. Lee, Y. Roichman and D. G. Grier, Opt. Express, **13**, 5831 (2005)

[40] Y. Roichman, A. S. Waldron, E. Gardel and D. G. Grier, App. Opt., **45**, 3425 (2005)

[41] J. D. Weeks, D. Chandler and H. C. Andersen, J. Chem. Phys., **54**, 5237 (1971)

[42] J. Rotne and S. Prager, J. Chem. Phys., **50**, 4831 (1969)

[43] M. Reichert and H. Stark, J. Phys. Condens. Matter, **16**, S4085 (2004)

[44] D. Frydel, Personal discussions

[45] J. Happel and H. Brenner, *Low Reynolds Number Hydrodynamics* (Martinus Nijhoff, The Hague, 1983), Sec. 6.4, p. 270

[46] J. Happel and H. Brenner, *Low Reynolds Number Hydrodynamics* (Martinus Nijhoff, The Hague, 1983), Sec. 5.11, p. 229